

This is the accepted manuscript made available via CHORUS. The article has been published as:

Anisotropic electron-phonon coupling investigated by ultrafast electron crystallography: Three-temperature model

Zhensheng Tao, Tzong-Ru T. Han, and Chong-Yu Ruan

Phys. Rev. B **87**, 235124 — Published 20 June 2013

DOI: [10.1103/PhysRevB.87.235124](https://doi.org/10.1103/PhysRevB.87.235124)

Anisotropic electron-phonon coupling investigated by ultrafast electron crystallography: Three-temperature model

Zhensheng Tao, Tzong-Ru T. Han, and Chong-Yu Ruan*

Physics and Astronomy Department, Michigan State University, East Lansing, Michigan 48824-2320

In low-dimensional electronic materials, the charge or spin ordering can be subtly controlled by specific mode or modes, giving rise to functioning states such as charge and spin-density waves, Mott insulators, and superconductors. The coupling between the electrons and the atomic lattice can be effectively investigated by ultrafast optical, photoemission, and electron diffraction techniques providing detailed description of microscopic and collective state evolutions in separate electronic and lattice subsystems. However, the electronic and phononic relaxation timescales obtained from these techniques are often distinctly different in low-dimensional electronic materials, even in system as simple as graphite. Here, we seek to understand their origins from examining the nonequilibrium scenarios considering anisotropic electron-phonon coupling leading to hot phonons, which can be investigated directly from the momentum-dependent scattering changes in the transmission ultrafast electron crystallography. A three-temperature model is constructed to achieve unified understandings combining ultrafast spectroscopy and diffraction results of the nonadiabatic optically driven dynamics in graphite, charge density waves in CeTe_3 , and Mott insulator VO_2 .

PACS numbers: 71.45.Lr, 63.20.kd, 71.27.+a, 78.47.J-

I. INTRODUCTION

Electronic phase transitions at low dimensions are generically associated with charge- and spin-orderings, but subtly controlled by a specific mode or modes well distinguished in momentum space¹. This is exemplified in charge-density wave (CDW) case, where the commonly held view is that CDW formation is mainly related to Fermi surface (FS) nesting², whereas more recent work has shown that strong electron-phonon and electron(hole)-electron couplings, in cooperation with lattice distortion and nesting, give rise to new classes of CDW in higher dimensions³⁻⁷. In the nesting driven scenario, the divergence of susceptibility is conveyed to coupled charge and lattice dynamics, known as Kohn anomaly, which freezes and forms CDW ground state at low temperatures as depicted in Fig. 1(a). Meanwhile, in the strong coupling limit, the momentum-dependent electron-phonon interaction leads to softening of lattice modes over an extended region in the Brillouin zone that doesn't match the best nested part of the FS, as evidenced in the CDW in 2H-NbSe_2 ³. Whereas different coupling mechanisms might be responsible, spectroscopy and diffraction are necessary tools to characterize the full parameter space of the cooperative state. For example, electronic ordering can be monitored through transient angular resolved photoemission (trARPES), which identifies the formation of an energy gap at q_{CDW} . Single-particle dynamics, the electronic temperature T_e can also be investigated via trARPES⁸⁻¹⁰, and combined with optical reflectance/transmission investigation, and terahertz (THz) spectroscopy^{11,12} yielding rich characterization data on the electronic evolution. Equally important are diffraction techniques¹³⁻¹⁵ to validate the critical coupling mode through tracking long-range ordering (amplitude and period) and short-range fluctuations of the lattice, necessary to describe the structure and dynamics in

the lattice counterpart¹⁶⁻¹⁸.

Recent trARPES studies of pristine 1T-TaS_2 , intercalated 1T-TaS_2 , and 1T-TiSe_2 , have shown subtle differences in the optical quenching timescales, which are used to explain their underlying different charge ordering mechanisms¹⁹. Yet, their respective relaxation timescales in relation to the energy transfer into the lattice and the CDW amplitude fluctuations have not been clarified, due to the probe's limited sensitivity to the lattice responses, although the nonhomogeneous phononic relaxation pathways are central to identify the electron-lattice couplings in these systems^{16-18,20}. Rather unexpectedly, following the fs quenching a nearly universal sub-ps (partial) recovery has been found from all-optical studies of various CDWs²¹. This phenomenon has recently been examined in details by Mihailovic and coworkers in a series of 1D, and 2D CDW systems, including TbTe_3 , DyTe_3 , 2H-TaSe_2 and $\text{K}_{0.3}\text{MoO}_3$, in the context of universality in the symmetry-breaking electronic phase transition²². The recovery of electronic order parameters was monitored by following the transient reflectivity in a series of three-pulses (destruction-pump-probe) experiment, where the CDW dynamics exhibit a common sequence of events: ultrafast quasi-particle gap recovery \rightarrow bosonic field amplitude fluctuations \rightarrow critical slowing down and domain creation. Such dynamics can be described simply on the basis of Ginzburg-Landau theory with the crystal ionic background treated as an effective vacuum, asserting that the sub-ps partial recovery of the CDW condensate may proceed independent of the details of the ionic state²¹.

In the ultrafast pump-probe studies of conventional metals and semiconductors, essential features of the experiments can be captured by the so-called two-temperature models (2TM)²³⁻²⁶, where the electronic (T_e) and lattice (T_l) temperatures are treated separately in timescale shorter than electron-phonon coupling time. In these materials, the injected optical energy dissipates

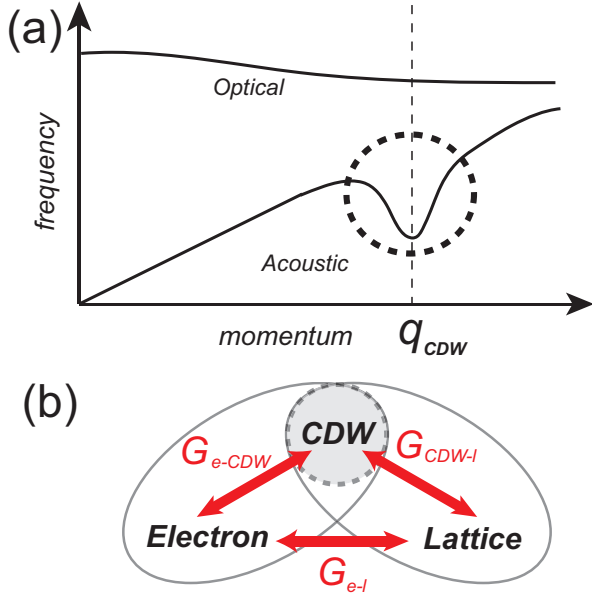


FIG. 1: (a) Phonon dispersion in charge-density wave (CDW) system, where a giant frequency reduction at the CDW wavevector q_{CDW} emerges. (b) The CDW collective state emerges by coupling in parts of the electronic and lattice momentum subspace near Fermi surface (FS), and stands out as an independent thermal reservoir. The couplings between the electron, lattice, and CDW are described by the three-temperature model, where G_{e-l} , G_{e-CDW} , and G_{CDW-l} describes the electron-lattice, electron-CDW, and CDW-lattice coupling constants.

in distinctive steps: first in the fs timescale the carriers establish a temperature (T_e) in the electronic subsystem, and at longer times (ps) the energy is transferred to the phonons, raising the lattice temperature (T_l). In such a thermodynamic view, optical pumping mimics the role of heating, allow ultrafast temperature jumps yielding non-equilibrium phases. However, in low-dimensional and correlated electron materials the energy transfer between the various degrees of freedom is far more complex. A simplistic extension of the two-temperature (T_e and T_l) description is the consideration of collective modes, which exchange energy with quasiparticles (e.g. electrons, spins, phonons etc.) in a highly energy and momentum selective manner²⁷, resulting in subsets of nonthermal baths among quasiparticles, such as hot phonons or hot spins. We use the CDW system as a prototypical example, where subsets of both electron and phonon baths are connected via collective modes, forming an independent thermal reservoir responding to energy transfer differently. This necessitates the three-temperature model (3TM) to describe the optical energy relaxations involving three-way couplings between the electron, lattice, and CDW as described in Fig. 1(b). We will show that allowing such a framework is crucial to reveal the subtle anisotropic coupling dynamics that is common to systems with low electronic dimensionality,

including CeTe₃, graphite, and VO₂.

II. METHODS

For describing the electronic subspace, optical and photoemission spectroscopies are well established^{11,12,28}. Here we focus on the concept of ultrafast electron crystallography (UEC) to characterize hot phonons dynamics. In UEC setup¹⁴, which is schematically described in Fig. 2(a), the probing electron pulses sample the lattice dynamics in a momentum-resolved manner. At each time frame by following the diffraction changes, the lattice responses in unitcell expansion/contraction (diffraction peak shift), atomic vibrations (diffraction intensity suppression), and loss of long-range ordering coherence (satellite intensity change) can be examined. For high-energy electrons (30-100 keV), the de Broglie wavelength λ_e is very short ($< 0.07\text{\AA}$), which gives a large Ewald radius ($R_{EW} = 2\pi/\lambda_e \geq 90\text{\AA}^{-1}$), which exposes a large section of the reciprocal lattice space for these investigations. The long-range-ordered states, such as charge-density waves, distort the primary lattice and form the superlattice, identified as the satellite reflections at spacing q_{CDW} surrounding the Bragg reflections. For describing these different structural orderings, the structure factor²⁹:

$$S(\mathbf{q}) = \sum_{\mathbf{G}} \sum_{n=-\infty}^{\infty} \delta[\mathbf{q} - (\mathbf{G} + n\mathbf{q}_{CDW})] J_n^2(A) F_n^\phi F_n^A F^P(\mathbf{G}) \quad (1)$$

gives diffraction intensity at different momentum transfer \mathbf{q} , where \mathbf{G} is the reciprocal lattice vector, A is the amplitude of the periodic lattice distortion induced by CDW, J_n is the Bessel function of the first kind of order n , describing the strength of the diffraction from superlattice ($n \geq 1$) or Bragg lattice ($n = 0$). These diffraction can be suppressed by atomic fluctuations, namely Debye-Waller (DW) factors: F_n^ϕ , F_n^A , and F^P . F_n^ϕ and F_n^A are associated with CDW superlattice, induced by the phase and amplitude fluctuations: δ_ϕ and δ_A respectively. More specifically, $F_n^\phi = \exp(-2n^2 W_\phi)$ where $W_\phi(T) = 1/2\langle \delta_\phi^2 \rangle$, and $F_n^A = \exp(-2(n^2 - |n|)W_A)$ where $W_A(T) = 1/2\langle \delta_A^2 \rangle$. The main Bragg reflections can be suppressed by $F^P = \exp(-\langle (\mathbf{G} \cdot \mathbf{u})^2 \rangle)$, induced by random atomic displacement u .

From analyzing these terms, UEC can be used for thermometry based on the known DW factors. Directly, from the relative intensity changes in the time-resolved diffraction intensity, a quantitative measure of the atomic fluctuational variance projected along \mathbf{G} can be determined, i.e. $\Delta\langle u_{\mathbf{G}}^2 \rangle = -\ln[I_{\mathbf{G}}(t)/I_{\mathbf{G}}(t < 0)]/|\mathbf{G}|^2$, where $I_{\mathbf{G}}(t)$ [$I_{\mathbf{G}}(t < 0)$] is the diffraction intensity after [before] laser excitation (at $t = 0$) obtained at \mathbf{G} . Because A can be easily determined from the superlattice intensity [J_n ($n \neq 0$) term], it is often used as an order parameter for CDW in the diffraction studies. The temporal correlations between different terms in Eqn. (1) exam-

ined in a large reciprocal space offer a bird's-eye view of intercorrelated electron-lattice, phonon-phonon interactions in complex systems. For example, it is interesting to investigate how the formation of uniaxial CDW [Fig. 2(b)] monitored from the recovery of superlattice intensity is coupled to lattice phonons, which can be analyzed through Bragg reflections.

Fig. 2(c) shows the UEC pattern of CeTe₃ obtained by directing the fs electron beam along the crystal orthorhombic b axis. The diffraction pattern not only records the nearly ideal 2D square host lattice, but also unveils the well defined CDW long-range order, as shown from the sharp satellite peaks highlighted in the inset at regions near (3,0) along the c -axis. The weak periodic distortion induced by the CDW ($\sim 0.1\text{\AA}$) gives a relatively low satellite intensity, 2-3 orders of magnitude lower than the intensity of the neighboring Bragg reflections¹⁸. In contrast, in the study of Mott insulator VO₂ the fs electron beam is directed along the crystal monoclinic b (b_M) axis³⁰ where strong dimer peaks emerge along the a_M -axis during metal-insulator transition. The insulating phase has the M1 structure as depicted in Fig. 2(d), generally perceived as derived from the more symmetric metallic rutile (R) structure through a Peierls-distortion that doubles the unitcell at the phase transition.

III. THREE-TEMPERATURE MODEL

Based on the respective diffraction intensities and DW factors, we can extract the temperature for the lattice

(T_l) and for hot phonons strongly tied to the CDW (T_{CDW}). In the three-temperature model (3TM) framework, T_l and T_{CDW} are linked to the electronic temperature T_e in differential equations tracking the decay of optical energy into electronic and nuclear manifolds. The size of the three energy reservoirs: electron, lattice, and CDW is gauged by their heat capacity, designated as C_e , C_l , and C_{CDW} respectively. The interactions between the three subsystems are described by the coupling constant G as depicted in Fig. 1(b). While this strategy has been used to model the temperature evolution of several related systems, such as graphite³¹, high-temperature superconductor³², and CDW systems^{7,18}, our approach here is different in that it explicitly takes into account the energy transport from the surface excited region into the bulk (along z) by diffusion. This is important to describe the depth profile of the optical excitation and the ensuing spatial-temporal evolutions of T_e , T_l , and T_{CDW} within the materials to create spatiotemporal evolution maps (see Fig. 3), necessary to quantitatively link the UEC experiments to the surface-sensitive photoemission and optical measurements. We use the electron and the phonon thermal conductivities K_e and K_l with a non-Fourier electronic relaxation time τ_e ²⁵ for diffusion and transport parametrization. The respective heat flux, q_e , q_l , and q_{CDW} , is driven by the temperature gradient. The coupled differential equations for 3TM with diffusion terms are described below (see Table I for the definition of the parameters used):

$$C_e \frac{\partial T_e}{\partial t} = -\frac{\partial q_e}{\partial z} - G_{e-l}(T_e - T_l) - G_{l-CDW}(T_e - T_{CDW}) + S(z, t) \quad (2)$$

$$\tau_e \frac{\partial q_e}{\partial t} + q_e = -K_e \frac{\partial T_e}{\partial z} \quad (3)$$

$$C_l \frac{\partial T_l}{\partial t} = -\frac{\partial q_l}{\partial z} + G_{e-l}(T_e - T_l) - G_{CDW-l}(T_l - T_{CDW}) - G_{l-env}(T_l - T_0) \quad (4)$$

$$q_l = -K_l \frac{\partial T_l}{\partial z} \quad (5)$$

$$C_{CDW} \frac{\partial T_{CDW}}{\partial t} = -\frac{\partial q_{CDW}}{\partial z} + G_{e-CDW}(T_e - T_{CDW}) + G_{CDW-l}(T_l - T_{CDW}) \quad (6)$$

$$q_{CDW} = -K_l \frac{\partial T_{CDW}}{\partial z} \quad (7)$$

, where $S(z, t)$ is the volumetric laser source term determined by the optical reflectivity R , the laser penetration

depth d_L , and laser pulse width t_p :

$$S(z, t) = \sqrt{\frac{4 \ln(2)}{\pi}} \frac{1-R}{t_p \times d_L} F \exp\left[-\frac{z}{d_L}\right] \exp\left[-4 \ln(2) \left(\frac{t-2t_p}{t_p}\right)^2\right]. \quad (8)$$

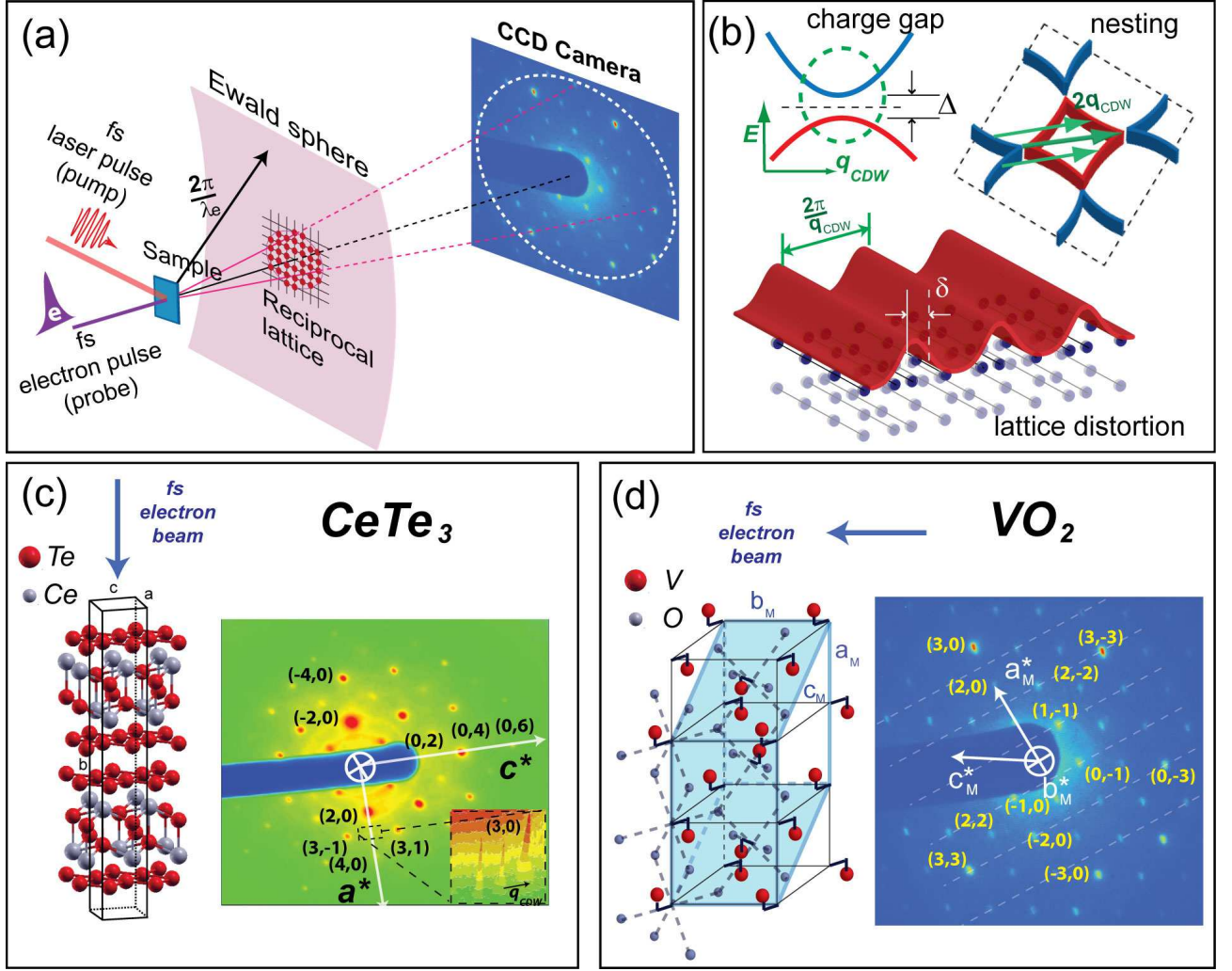


FIG. 2: (Color online) (a) Conceptual depiction of the laser pump and electron probe arrangement of ultrafast electron crystallography (UEC). The large Ewald sphere, defined by the sub-angstrom de Broglie wavelength of the electron λ_e , intercepts a large cross-section of the reciprocal lattice of the sample crystal in the transmission geometry, defining the diffraction zones. The diffraction pattern is projected in the far field on a charge-coupled device (CCD). (b) The Fermi surface (FS) sheets of a 2D lattice, hosting a uniaxial charge-density wave at q_{CDW} . The nesting at $2q_{CDW}$ from one corner of the Fermi sheet to another, connecting large parallel portion of the FS, can be seen. The formation of CDW induces a single-particle gap Δ at FS, and periodic lattice distortion δ at q_{CDW} . (c) The probing of $CeTe_3$ lattice by UEC. The fs electron beam impinges the crystal along the rhombohedral b -axis, exposing square ac reciprocal lattice, in which the existence of a charge-density wave can be seen in the presence of satellite at q_{CDW} from the main reflections. The inset shows the sharp CDW satellites near the $(3,0)$ reflection. (d) The probing of VO_2 lattice by UEC. The fs electron beam impinges the crystal along the monoclinic b -axis, exposing nearly triangular ac reciprocal lattice. The structural phase transition can be characterized as lattice dimerizes along the a axis, creating additional reflection peaks (dash-lines).

The initial and boundary conditions are defined by

$$T_e(z, 0) = T_l(z, 0) = T_{CDW}(z, 0) = T_0 \quad (9)$$

$$q_e(0, t) = q_l(0, t) = q_{CDW}(0, t) = 0 \quad (10)$$

$$q_e(L, t) = q_l(L, t) = q_{CDW}(L, t) = 0 \quad (11)$$

These equations are numerically solved with the MacCormack method³⁹. The coupling constants G_{e-l} , G_{e-CDW} , and G_{CDW-l} for the electron-lattice, electron-CDW, and CDW-lattice interaction respectively are de-

termined by fitting the experimental data, whereas the materials parameters C_e , C_{tot} , K_e , K_l are treated as inputs using the literature values (see table I). In addition, we use the partition factor α to determine the relative size of the CDW and the lattice sub-spaces in the overall nuclear heat capacity C_{tot} :

$$C_{CDW} = \alpha C_{tot}, \quad (12)$$

$$C_l = (1 - \alpha) C_{tot}. \quad (13)$$

α affects mainly the temperature ratio between the CDW and the lattice, and it can be gauged by fitting. The coupling constant and the heat capacity jointly affect the relaxation timescale, which is easily seen from Eqns. (2), (4) and (6), where the C/G is related to the timescale of the coupling between two subsystems. Results from ultrafast spectroscopy and diffraction are combined to validate the full coupling hierarchy. Specifically, we rely on the ultrafast optical and photoemission techniques to

provide information on the electronic evolutions, i.e. T_e and quench/recovery dynamics of the charge gap. We rely on the momentum-dependent UEC studies for evaluating T_{CDW} , T_l , and quench/recovery dynamics of structural order parameter. In the followings, we use 3TM to characterize the three prototypical hot phonon systems: CeTe₃, graphite, and VO₂, and seek to understand the origins of hot phonons and their relationship to the specific electron-phonon coupling hierarchy in these systems.

TABLE I: Three-temperature model parameters

Name	Meaning	Parameters used for CeTe ₃
$C_e = \gamma T_e$	Electron heat capacity	$\gamma = 11.3 \text{ J m}^{-3} \text{ K}^{-233}$
τ_e	Electron relaxation time	$\tau_e = 100 \text{ fs}^{25}$
$K_e = LrtzT_e/\rho^{35}$	Electron thermal conductivity	$\rho = 2.0 \times 10^{-5} \Omega \text{ m}^{36,37}$
K_l	Lattice thermal conductivity	$K_l = 0.5 \text{ W m}^{-1} \text{ K}^{-138}$
C_{tot}	Total nuclear heat capacity	$C_l = 1.317 \times 10^6 \text{ J m}^{-3} \text{ K}^{-133}$

IV. IV. OPTICALLY DRIVEN PHASE TRANSITION OF 2D CDW IN CETE₃

We choose CDW in CeTe₃ as our first model system in that it represents a canonical system to study the anisotropic electron-phonon coupling. The formation of a uniaxial CDW (along c -axis) in the nearly ideal 2D metallic Te square nets provides us a clear handle to monitor the symmetry breaking induced by CDW through comparing the a - and the c -axis responses. Any deviation detected in the dynamics along the c -axis from that along the a -axis is expected to link to the CDW formation [Fig. 2(c)]. The optically driven phase transition of the rare-earth tritelluride systems has been recently investigated using UEC¹⁸, trARPES⁸, and ultrafast optical reflectivity²² techniques. The intertwined nature of the relaxation processes is reflected in the distinct relaxation timescales from different probes. In Fig. 3(a), the inset shows the UEC results for T_l and T_{CDW} , obtained by monitoring the anisotropic phononic responses (Debye-Waller analysis)¹⁸. The main panel shows that the electronic temperature (T_e) extracted from trARPES⁸ is closely complementary to T_{CDW} extracted from UEC. This means that the photoexcited carriers are strongly coupled to the CDW collective modes, whereas the much weaker coupling to the lattice forms a bottleneck in thermal energy redistribution to all the lattice modes, leading to a slow T_l rise.

Three-temperature model provides detailed analysis of T_e , T_l , and T_{CDW} in a self-consistent manner using the UEC results from a given optical energy absorption, which defines the initial overall energy deposition. Fig. 3(b) shows the space- and time-resolved temperature

map and order parameter dynamics deduced from the three-temperature model. The data obtained at the fluence $F=2.43 \text{ mJ/cm}^2$ are reproduced as square dots (for complete results at different fluences, see reference¹⁸). The modeling is based on fitting T_{CDW} and T_l with the parameters $\alpha=0.33$, $G_{l-env}=3.4 \times 10^{14} \text{ Wm}^{-3} \text{ K}^{-1}$ (constrained independently by the long-time data showing 2.7 ns decay time of T_l), $G_{e-l}=2 \times 10^{14} \text{ Wm}^{-3} \text{ K}^{-1}$, $G_{e-CDW}=8.5 \times 10^{15} \text{ Wm}^{-3} \text{ K}^{-1}$, and $G_{CDW-l}=1.2 \times 10^{16} \text{ Wm}^{-3} \text{ K}^{-1}$. We note that without conforming to T_l α may vary from 0.05 to 0.33 in keeping the quality of fits with G_{e-CDW} remaining the same and G_{e-l} and G_{CDW-l} weakly changing with respect to α . The backgrounds in the panels of Fig. 3(b) depict the spatial and temporal evolutions modeled by 3TM. The solid lines are the bulk-averaged (integrated from $z=0$ -50 nm) for modeling the UEC data. The dash-lines show the temperatures and the CDW order parameter modeled at the surface ($z=0$ nm), which are directly relevant to trARPES and optical studies. We show that T_e from fitting to UEC data (black solid line) is very consistent with T_e from trARPES (pink dash-line). The different timescales of T_{CDW} , T_l , and T_e obtained using diffraction and electron spectroscopy can be reconciled by considering the momentum-dependent electron-phonon coupling. Meanwhile, the optical result (blue dash-line), which exhibits a sub-ps decay, is quite different from the timescales of both T_e and T_l . As already been pointed out, the transient optical techniques detect the pump-induced changes (reflectivity, transmission, or conductivity), which can be driven by quasiparticle kinetic energy, as in conventional metals and semiconductors, as well as the electron self-energy and pairing self-energy in correlated electron sys-

tems or systems with collective ground state^{11,12}. The specific optical timescale may trace its origin to the CDW collective state evolution^{21,34}.

Important insight on the CDWs properties can be gained by examining the dynamics projected in their order parameters [optical gap Δ and lattice distortion A , see Fig. 2(b)] and comparing them with the quasiparticle temperature evolutions (T_e , T_{CDW} , T_l), which are mediated by the respective coupling strength between electrons, CDW, and lattice. In UEC, the CDW order parameter evolution tied to symmetry change directly alters the superlattice intensity. Meanwhile, the loss of the spatial coherence (phase and amplitude modes) generally suppresses the superlattice intensity. These two processes have well distinguished timescales and can find matches in the respective timescales from optical and photoemission studies, offering corresponding electronic responses during the same period. First, the order parameter A captures a sub-ps partial recovery, which is well related in timescale to the reopening of Δ established from the trARPES⁸, and also to the optical recovery (quasiparticle lifetime) measured in the optical three-pulse (destruction-pump-probe) experiment²². The prominent ps dynamics captured in UEC is well linked to T_e decay seen in trARPES, but not shown in the three-pulse optical study. The slower phonon-mediated electronic cooling observed here clearly indicates that the sub-ps quasiparticle recovery is purely electronic in nature, driven by the interaction between hot carriers and CDW condensate, which is indeed commonly found in several CDW systems (DyTe₃, 2H-TaSe₂, and K_{0.3}MoO₃)²² with very different electron-phonon coupling strength^{21,40}. On the other hand, 3TM determines, by deconvoluting the diffusion effect and excitation depth dependence, a timescale for the satellite intensity's initial recovery on the surface [as shown in dash-line in the lower-right panel of Fig. 3(b)] nearly identical to the optical result. Given this agreement the initial recovery of the superlattice intensity might be attributed to the reinstatement of the overall phase coherence of the charge condensate. This view (namely, electronic quench/recovery) is further supported by the saturation behavior observed only in the fast component, whereas beyond $F \sim 4$ mJ/cm² [Fig. 4(a) in reference¹⁸] the change is nearly constant. This fluence threshold is equivalent to the energy required to destroy the charge condensate. After deconvoluting the depth-dependence a surface critical fluence of ~ 2 mJ/cm² is determined, in very good agreement with the trARPES result⁸.

The large disparity between G_{e-l} and G_{e-CDW} deduced using 3TM supports that electron-phonon coupling plays a direct role in stabilizing the CDW ground state⁴. A fundamental issue is the role of FS nesting in leading to this asymmetry. Indeed, an electronic structure calculation (assuming $a=c$) has shown a small asymmetry in the splitting of FS sheets owing to coupling between the two nonequivalent square Te nets. However, such weak perturbation is not large enough to account for the

observed strong electron-phonon anisotropy in the CDW ground state⁴¹. This is supported by a steady-state Raman investigation of ErTe₃ where nearly symmetric responses along the a and c axes were found at above the CDW transition temperature⁴². An alternate symmetry-breaking picture was proposed with the idea that the CDW formation might be initially triggered by the weak FS asymmetry, but subsequently stabilized by a focusing effect introduced by hybridization between two perpendicular in-plane p-orbitals and a strong electron-phonon coupling⁴². It would be extremely interesting to explore this dynamical symmetry-breaking scenario in systems that are inherently symmetric, such as rare-earth ditelluride compounds, to see whether CDW can be switched into a different axis by the laser pulses.

This 3TM study represents a step forward in clarifying different results obtained from optical, photoemission, and electron diffraction regarding the interplay between charge and structural order parameters and how the hot phonons help drive the structural phase transition. Through accurately predicting T_e , the nonequilibrium charge and lattice dynamics in the reconstitution of a quenched 2D charge-density wave are reconciled in a self-consistent way. By relating the optical results to the lattice dynamics, we have demonstrated that the collective state formation within the 2D metallic rare-earth tritelluride compounds has a major effect on the optical reflectivity, which sensitively captures the recovery of charge ordering^{11,21,22}. This essential feature is somewhat different at lower fluences where the more dominant ps component describes the quasi-particle dynamics rendered by carrier-phonon and phonon-phonon interactions^{21,43}. This shows the importance of exploring different techniques in tracking the full parameter space, including electron and lattice, in order to put together a complete picture for the intercorrelated couplings with strong anisotropy in 2D systems.

V. 3TM MODELING OF ELECTRON AND LATTICE DYNAMICS IN GRAPHITE

Graphite is a semi-metal with its electronic properties largely defined by the 2D honeycomb structure and weak perturbations from van der Waals layers that create a small bandgap at FS. The electron-phonon coupling is a fundamental bottleneck for ballistic transport in graphene and carbon nanotubes, and recently in optical studies of graphite anomalous quasiparticle lifetime and hot carrier-optical phonon scattering mechanism have been called into questions^{31,44,45}. The transient optical and spectroscopic studies of graphite are indeed intriguing as generally fs recoveries were obtained in optical reflectivity and the transmittance measurements⁴⁶⁻⁴⁸, whereas in transient terahertz (THz)³¹ and photoemission studies⁴⁵ much longer hot carrier cooling times (ps) were observed. For comparison, the T_e measurement from transient photoemission spectroscopy conducted at

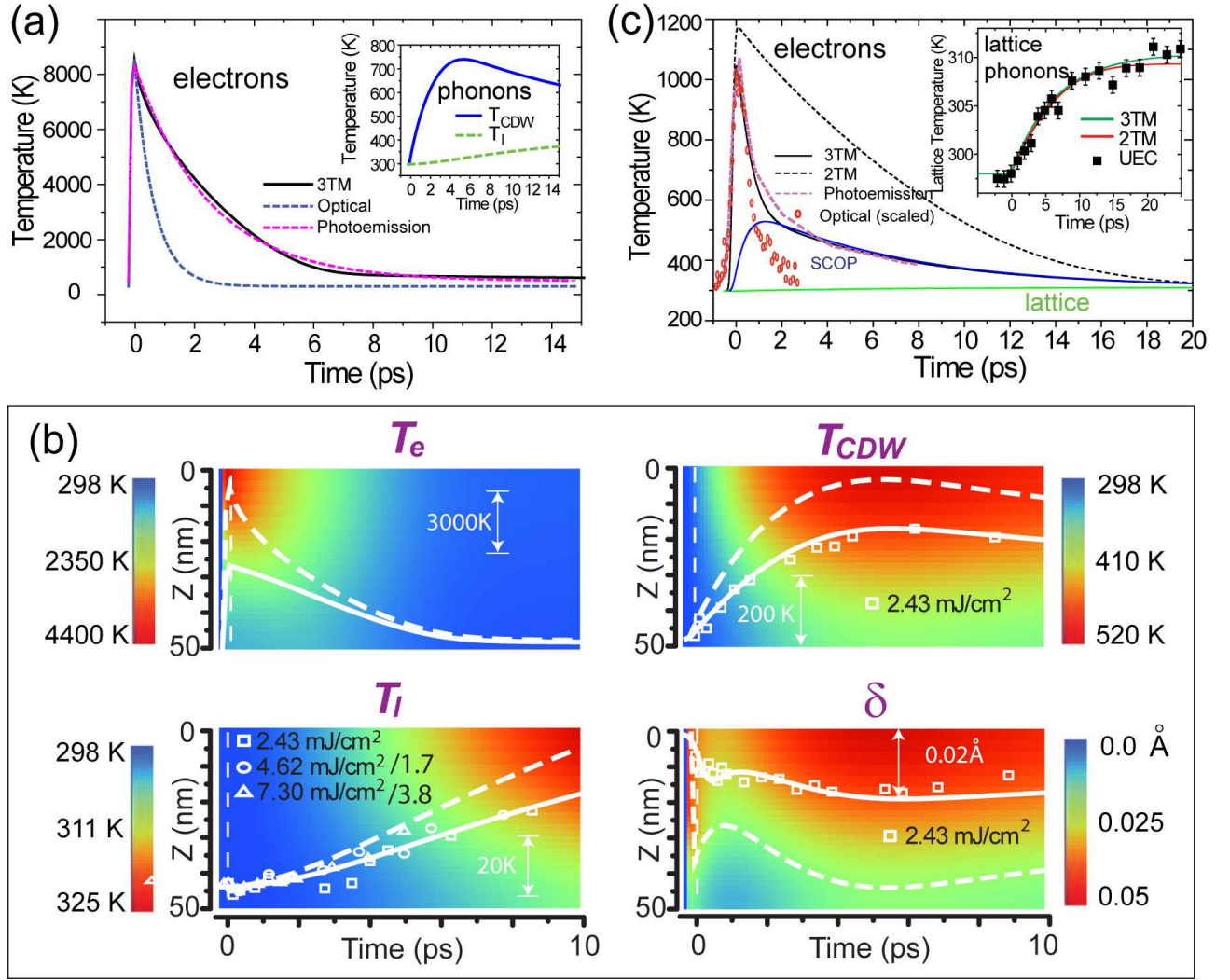


FIG. 3: (Color online) Three-temperature model. (a) The electronic temperature T_e deduced from ultrafast electron crystallography (UEC) experiments based on 3TM for CeTe₃, compared with the results reproduced from optical and photoemission studies. The inset shows the CDW-associated phonons and lattice temperatures. (b) The spatial and temporal evolution of the electronic, CDW, and lattice temperatures: T_e , T_{CDW} , T_l , and order parameter A respectively, based on the three-temperature model. The dynamics of A is modeled after phase and amplitude modes¹⁸. Solid lines represent the bulk-averaged ($z=0$ to 50 nm) value, and dash-lines represent the surface ($z=0$ nm) value. The symbols are the corresponding experimental results from UEC. (c) The three-temperature model (3TM) and the two-temperature model (2TM) of graphite, compared with optical reflectivity and results reproduced from photoemission study⁴⁵. The temperature of the strongly coupled optical mode (SCOP) and that of the lattice calculated by the three-temperature model are also shown for comparison. The inset shows the UEC results of the lattice temperature, which constrain the two-temperature and three-temperature modelings.

$F=64 \mu\text{J}/\text{cm}^{245}$ is reproduced in Fig. 3(c) (purple dash-line) together with the transient optical reflectivity (circles) and UEC (solid squares) data we obtained on graphite. All these experiments were performed using 800 nm fs laser pulses as the excitation source.

While the electron-phonon coupling in graphite is believed to be smaller than normal metals⁴⁹, a large coupling constant is usually required for explaining fs laser^{31,45,50} and swift ion-beam irradiation experiments^{51,52}. This discrepancy reveals a complex energy exchange in nonthermally heated graphite when

compared to conventional metals. The large electron-phonon coupling observed for optically pumped high energy carriers have been attributed to the strongly coupled optical phonons (SCOPs)^{31,45,47,50}. Their unusual coupling strength to the electrons has also been linked to anonymous phonon dispersion (Kohn anomaly) at Γ and $K(K')$ points taking into account the long-range character of dynamical electron-phonon coupling matrix^{53,54}.

Insight on the energy relaxation pathways involving such SCOPs can be gained from examining a recent steady-state photoemission study⁵⁵, where photoelec-

trons appear around the Γ region, even though there is no band around Γ in the vicinity of Fermi level (E_F). The most obvious explanation is that photoelectrons can be efficiently scattered into the Γ region by high-energy optical phonons. Yet, two puzzling observations remain. First, the T_e obtained from the THz³¹ and photoemission⁴⁵ studies appear to be significantly lower than the prediction from the two-temperature model (2TM). Such interesting observation has led to the assumption that SCOPs might be involved in the carrier generation process to directly channel optical energy into the lattice^{31,45}. Second, the various timescales reported for hot phonon relaxations, which range from 1 to 7 ps^{31,48,56} must be reconciled with the time scale of lattice heating^{57–59}.

Unambiguously, from comparing the T_e data from photoemission and the T_l data from UEC as presented in Fig. 3(c), an intermediate step for energy transfer must exist. The sub-ps decay of T_e is too fast to directly lead the ps rise of T_l , and we might attribute this dark intermediate step as due to in-plane SCOPs as suggested from the optical studies^{31,45,56,60,61}. This scenario is akin to the CDW case, where the first step of electronic energy relaxation is coupled to selected modes. The important remaining issues are to determine the extent of the thermal bath associated to SCOPs and whether the coupling to SCOP from optical excitation is direct or subsequent to the electronic excitation. In 3TM, the SCOPs are treated as an independent thermal reservoir from the lattice (with temperature T_{SCOP} , heat capacity C_{SCOP}). In extracting the temperatures, T_l is calculated based on in-plane atomic fluctuation variance in ultrathin graphite nano-platelets (≈ 10 nm) obtained from UEC using the tabulated Debye-Waller factor⁶². To be consistent with the photoemission result, the lattice temperature is linearly scaled down to match the photoemission data from ~ 1 mJ/cm² region. The energy transfer to the lattice is nearly sequential given the disparate energy decay timescales: ~ 500 fs from electrons to SCOP (photoemission), and ~ 7 ps from SCOP to the lattice (UEC). From 3TM modeling, corresponding G values ($G_{e-l}=0.2\times 10^{16}$ Wm⁻³K⁻¹, $G_{e-SCOP}=1.6\times 10^{16}$ Wm⁻³K⁻¹, and $G_{SCOP-l}=1.3\times 10^{16}$ Wm⁻³K⁻¹) are determined. In addition, from fitting the T_e and T_l based on the absorbed optical energy, we determine the size of the SCOP to be a small subset of the overall phonon bath ($C_{SCOP}=5.5\times 10^4$ Jm⁻³ K⁻¹; total nuclear heat capacity $C_{tot}=1.56\times 10^6$ Jm⁻³ K⁻¹). Ignoring the existence of SCOP, as shown in the 2TM simulation, the prediction [dash-line in Fig. 3(c)] fails not only to reconcile with the measured dynamics, but also the energy scales of T_e and T_l .

From the 3TM, we also deduce the electronic heat capacity in terms of $C_e = \gamma T_e$. The best fitted γ value is 30 Jm⁻³K⁻², which is an order of magnitude higher than the steady-state value ($\gamma_0=2.4$ Jm⁻³K⁻²)⁶³. This high γ value is required to generate the somewhat surprising lower-than-expected T_e as determined from photoemis-

sion [Fig. 3(c)]⁴⁵ and THz³¹ measurements. Based on free electron Fermi gas model²⁶, the increase of electron heat capacity can be traced to the increase of free carrier density, which, in the case here, is induced by optical excitation. The instantaneous photo-carrier concentration can be estimated from $n_{op} \sim F(1-R)/(d_L h\nu)$. Using the experimental parameters: $F=64$ μ J/cm², $h\nu=1.55$ eV, $R=0.3$, and $d_L=30$ nm⁴⁶, we obtain $n_{op} \sim 10^{26}$ m⁻³ (electrons and holes combined). This is indeed one order of magnitude higher than the reported intrinsic carrier concentration $n_i \sim 10^{25}$ m⁻³⁶⁴. This could explain the large electronic heat capacity without invoking the scenario where SCOPs are directly involved in the carrier generation process and participate the early stage of energy sharing of the absorbed optical energy.

Possible identities of the SCOPs have been proposed from several optical pump-probe experiments based on identifying hot phonons that are closely coupled to the photoexcited carriers. They are: Γ -point E_{2g2} mode (in-plane stretching, 200 meV)^{56,60}, E_{2g1} mode (inter-layer shearing, 6 meV)⁶¹, and optically dark K(K')-point modes (out-of-plane, 67 meV; in-plane, ~ 160 meV)^{45,53,55}. In particular, the high-energy in-plane Γ -point and K(K')-point modes are also likely participants responsible for significant reduction of the ballistic conductance of carbon nanotubes and graphene at bias potentials larger than 0.2 V^{65–71}. In terms of timescales, we note that the average lattice heating time of ~ 7 ps determined from UEC is similar to the SCOP thermalization time deduced from THz study³¹, and consistent with the ps component of T_e determined from photoemission⁴⁵. First principle calculation was able to attribute this timescale to overall SCOP-lattice thermalization from various active optical phonon decay channels⁷². A recent UEC investigation of graphite film (1-3nm)⁵⁷ reported a two-step (700 fs, 12 ps) decrease of diffraction intensity and attributed them to initial decay from K(K') point and phonon thermalization respectively. We note that the lattice temperature is based on the random atomic fluctuational variance deduced from DW analysis on diffraction intensity changes, which in an equilibrium condition is linked to a thermal mode (j) with $\langle u_j^2 \rangle \sim k_B T_j / m_e \omega_j^2$. One can easily see in this thermal case the displacement variance $\langle u_j^2 \rangle$ at a given temperature is inversely proportional to the frequency of the phonon squared ω_j^2 , therefore the sensitive of detecting the high-frequency SCOP based on diffraction intensity changes is highly suppressed – for example, ~ 47 THz E_{2g2} mode is three-orders of magnitude more difficult to see than 1.4 THz interlayer shearing mode given the same energy transfer. Meanwhile, if the initial coupling results in coherent SCOPs⁶⁰, the changes should be in the diffraction width rather than the integrated intensity. These two scenarios explain why in our analysis of UEC data the high-frequency SCOP responses are largely undetected. We note that unlike the previous UEC experiment we are not able to ascertain the sub-ps component in the initial decay of diffraction intensity, this might be

attributed to the difference in our samples (mode-mode couplings have been found to depend on the sample thickness, size, and morphology^{48,73}) or the model used in fitting, which should be verified in future experiments. We also note that in this experiment the excitation fluence is kept low so the maximum photocarrier generation is less than 1%. It is worth mentioning that c -axis lattice dynamics^{58,74}, $sp^2 - sp^3$ bonding changes^{58,75}, and even band gap renormalization⁷³ have been reported under more intense laser fluences where $n_{op} \geq 10^{27} \text{m}^{-3}$, or up to 10% of electrons, are excited from π to π^* band. Under this strongly perturbed situation new or different channels of electron-lattice interaction can emerge due to changes in electronic structure and/or charge redistribution between graphitic layers^{58,76}, which is a rather interesting subject on its own.

In summarizing this section, we have clearly demonstrated the need to consider strongly coupled modes as an intermediate step to transfer the optical energy to the lattice based on three-temperature model. We determine the size of these SCOPs to be merely $\sim 3.5\%$ of the total lattice heat capacity. The lack of significant SCOP features in UEC diffraction images suggest that they are high-frequency optical modes in nature. A simple free electron gas model explains the relative low T_e as due to dramatic increase in free carrier concentration from optical excitation. Nonetheless, this model requires a step-wise sequence of carrier generation and electronic thermalization to occur. If the two processes occur concurrently, the prediction of T_e will be higher, hence additional heat capacity from the SCOP will be required in order to account for the moderate T_e observed⁴⁵. Whether there is a direct nonthermal transfer of the optical energy to SCOP as part of the initial accepting thermal reservoir will require further UEC experiments to be conducted on single crystal graphite with large lattice persistence length to separate the average thermal lattice heating from the excitation of the selected SCOP, which would be expressed as momentum-dependent correlated modulations of the lattice Bragg intensity or width on ≤ 1 ps timescale.

VI. VI. ANISOTROPIC LATTICE DYNAMICS IN VO₂ NEAR METAL-INSULATOR TRANSITION

VO₂ represents a prototypical system for studying metal-insulator transition (MIT) in correlated electron materials. Despite of its simplistic atomic composition, VO₂ exhibits complex electronic and structural phase diagrams^{77,78}. Like in many correlated electron materials, MIT in VO₂ is subject to intertwined control parameters (e.g. stress, heat, doping, field, and optical excitations), but generally MIT is seen to strongly couple to rutile-to-monoclinic structural phase transition. At low temperatures, VO₂ is insulating and monoclinic (M1) [Fig. 2(d)]. Heating VO₂ above the insulator-metal phase

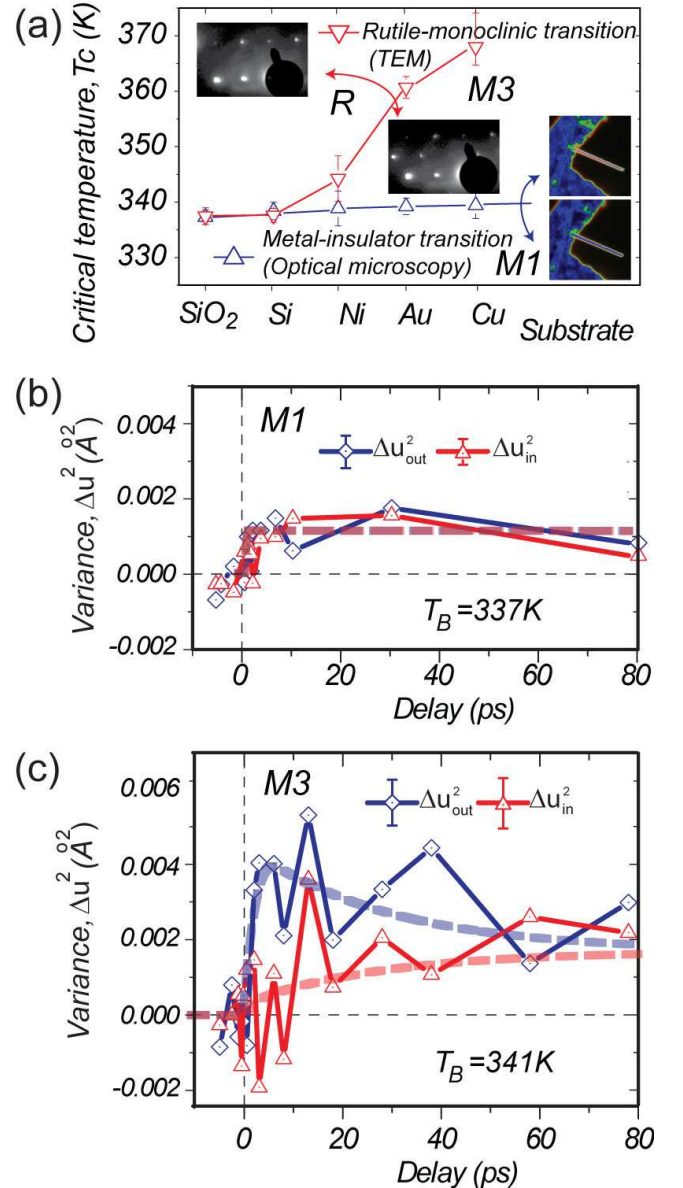


FIG. 4: (Color online) (a) The phase diagram of VO₂ phase transitions on different substrates. On insulating surface the transition is cooperative with metal-insulator transition (MIT) occurring simultaneously with rutile-monoclinic transition. On metal surface the structural transition is upshifted from MIT, exposing an intermediate regime with monoclinic metallic phase (M3). (b) The atomic fluctuational variance determined for Au-supported VO₂ in the M1 state ($T_B = 337$ K). (c) The atomic fluctuational variance determined for Au-supported VO₂ in the M3 state ($T_B = 341$ K). The dash-lines are results from three-temperature modeling.

transition temperature T_c (~ 340 K) results in a sharp increase in electrical conductivity accompanied by a relaxation of the lattice to a rutile (R) structure. However, unlike in CDW systems, this cooperativity can not be reduced to a simple coupling between the free carriers and the lattice to form a cooperative state. In

VO₂, the change in electron occupancy can dynamically shift bands due to strong electron correlation effects driving electronic phase transition. While it is largely accepted that both electron-electron and electron-phonon interactions are at plays, considerable debates over the precise origins of phase transitions, namely as due to electronic instability (Peierls-Mott) or Peierls instability (Mott-Peierls), are evident in recent experimental^{79–91}, and theoretical^{92–95} literatures. Therefore, delineating the respective roles of the electron-phonon and electron-electron interactions in driving the structural and electronic phase transitions is central to address the open issues.

Most recent experiments in single-crystal VO₂ nanobeams³⁰ and VO₂ field effect transistor (VO₂-FET)¹⁰⁰ have presented clear evidences of a metallic monoclinic state under electrostatic doping, which has challenged the commonly held view of rigid macroscopic cooperativity between structural and electronic phase transitions. In recent VO₂ nanobeam experiments, the lattice strain has been used as a controlled parameter to study phase transition^{96–99}. Conversely, at nearly strain-free condition, sharp transition can be achieved, allowing inherent properties associated with electron-electron and electron-phonon interactions to be carefully examined. Indeed, combining optical and electron microscopy the electronic and structural phase transitions of VO₂ nanobeams have been investigated, where T_c of structural transition was identified as upshifted from that of the MIT when nanobeams were gently placed on metal surfaces (see Fig. 4(a))³⁰. The intermediate monoclinic metal state is designated as M3 to distinguish it from the insulating M1 state. The M3 state occurs most prominently in short nanobeams where nearly strain-free condition can be readily achieved, but the large shift in T_c can only be seen on metal surfaces, which is explained as induced by interfacial charge doping³⁰. Similarly, in VO₂-FET experiment, the MIT in the VO₂ channel occurs under gate-doping using ionic liquid, but the induced metallic state retains a monoclinic structure¹⁰⁰. Different from the nanobeam experiments, the VO₂ channel in VO₂-FET is highly strained and the MIT occurs only under a high electric field, indicating the need to overcome strain energy before macroscopic switching occurs¹⁰⁰. Interestingly, by increasing the gate field, the monoclinic VO₂ becomes even more distorted. Also in earlier channel experiments the MITs from monitoring resistivity were found to decouple from structural phase transition^{101,102}. Generally in these experiments, the electrostatic doping, achieved by introducing carriers into the conduction band, stabilizes the monoclinic phase, and consequently the MIT, driven by temperature or potential, can occur without obviously changing lattice translational symmetry. However, if phonons are involved as the system changes from metal to insulator, the electron-phonon coupling will drive active modes. Without this cooperativity, the electron-electron and electron-phonon interactions might be seen as separate mechanisms medi-

ating MIT and Peierls distortion in the electrostatically doped VO₂.

Using ultrafast electron crystallography, the active phonon modes are tracked by conducting experiments on a gold-supported VO₂ beam above and below the electronic phase transition while keeping the monoclinic structure. The experimental geometry is defined in Fig. 2(d) with probing electron pulses directed along the b_M axis. From UEC, the atomic fluctuational variance normal to the $b_M - c_M$ plane (designated as Δu_{out}^2) and along the $b_M - c_M$ plane (designated as Δu_{in}^2) can be deduced. These values can then be translated into temperatures using the tabulated DW factors of VO₂^{103–105}. Using 3TM, we keep track of the optical energy that decays into thermal energies in the electronic and lattice reservoirs, according to the optical absorbance and the respective electron-phonon and phonon-phonon couplings. The experimental results are depicted in Fig. 4(b&c), where Fig. 4(b) shows the fluctuational variances Δu_{in}^2 and Δu_{out}^2 determined below the T_c , and Fig. 4(c) shows the results just above T_c . In these experiments the excitation fluence ($F=7$ mJ/cm²) and photon energy (1.55 eV) were kept the same. In the insulating M1 ground state, the electron-phonon coupling is found to be more isotropic, whereas in the M3 metallic state a change in coupling hierarchy is clearly visible with hot phonons being generated at early times along the pairing direction. Much like in the case of CDW, these hot phonons couple strongly to the electronic excitation and their decays lead to heating of the overall lattice in over 80 ps. These distinct results support that the M1-M3 electronic phase transition is coupled to the lattice microscopically without changing its symmetry macroscopically¹⁰⁶.

In the 3TM modeling, we associate Δu_{out}^2 to SCOP with $\alpha=1/3$ based on M1 symmetry and the experimental phononic responses. The coupling constants between electrons and different subsets of phonons (namely, lattice and SCOP) change drastically across MIT. In M1 state, $G_{e-l}=3\times 10^{16}$ Wm⁻³K⁻¹. In M3 state, $G_{e-l}=0.2\pm 0.1\times 10^{16}$ Wm⁻³K⁻¹ (large uncertainty due to the significant scattering of Δu_{in}^2 data), $G_{e-SCOP}=1.1\times 10^{16}$ Wm⁻³K⁻¹, and $G_{SCOP-l}=1.8\times 10^{16}$ Wm⁻³K⁻¹). Additionally, from matching the lattice temperature and the T_e deduced based on optical absorbance⁷⁹ in 3TM, we find that in the electrostatically doped VO₂ the penetration depth lengthens significantly from (~ 127 nm⁷⁹) in the undoped system to $\gg 200$ nm in the electrostatically doped case. This implies an increase in the optical gap energy due to doping. Since the emerging active modes along the pairing axis occupy full 1/3 of the nuclear heat capacity, the lattice has become more 1D-like after the transition. This phononic realization of changing energy landscape is consistent with the X-ray absorption and photoemission results reporting a dynamical shift of spectral weight in favor of Peierls bands following MIT^{81,82}. Such a shift is expected as further gap opening can be

explained through an enhanced Peierls interaction in a structure with more 1D-like bands. This conclusion is also consistent with the VO₂-FET experiment where a more Peierls-distorted structure occurs under a stronger gate-doping¹⁰⁰. Based on these results, we suggest that Peierls interaction plays a key role in mediating the optical gap opening whilst being influenced by the dynamical switching induced by electron correlation effects^{93,95}. As to the changes in the electrical conductivity during MIT, it is generally mediated at a lower energy scale and may be solely driven by the Mott physics. Direct confirmation of these conclusions will require additional spectroscopy and UEC experiments to look for subtle changes at lower energy scale than optical gap during MIT.

Using 3TM we have examined the electron-phonon coupling in the electrostatically doped VO₂ system and demonstrated a clear change in the electron-phonon coupling hierarchy during MIT. Even though the host VO₂ lattice structure does not attain different crystalline symmetry explicitly (both M1 and M3 are in the low symmetry configuration), the electrostatic doping is seen as strengthening the Peierls characters. Other doping-induced decoupling of structural and electronic phase transitions have indeed been observed. For example, in the parent compounds of iron pnictide high-temperature superconductor, with BaFe₂As₂ as a prototypical example, the magnetic phase transition (antiferromagnetic spin order to non-Fermi liquid) is always accompanied by the tetragonal-to-orthorhombic structural phase transition¹⁰⁷. On the other hand, in the doped regime near high-temperature superconducting phase, the critical temperature of the magnetic phase transition is slightly below that of the structural phase transition¹⁰⁸, as in metal-supported VO₂. On the microscopic level, the connection between anisotropic electron-phonon coupling and electronic phase transition seems to be general, as such evidences also have been found in recent ultrafast optical^{11,109}, electron diffraction^{32,110} and ARPES^{28,111,112} studies of high- T_c superconductors with signatures of momentum-dependent decays of electrons indicative of an anisotropic electron-boson coupling enhanced by the presence of superconductivity.

VII. VII. SUMMARIES AND PERSPECTIVES

The three-temperature model has been applied to investigate the electron-phonon mechanism in three classes of low-dimensional systems (CeTe₃, graphite, and VO₂) using data obtained from multiple techniques, including transient optics, momentum-resolved photoemission spectroscopy, and ultrafast electron diffraction, by tracking the electronic and nuclear (lattice) energies following optical excitation. All of these materials have reduced electronic dimensionality and exhibit anisotropic electron-lattice interaction that is not seen in conventional semiconductors and metals. Three-temperature model is essential to tie the optical, electronic, and nu-

clear energies together in order to deduce coupling constants from comparing the momentum-resolved temporal evolutions of electronic and phononic temperatures, in relation to the evolutions of collective states in both electronic and lattice subsystems. The formation of collective state is seen as central to induce large anisotropy in lattice fluctuational responses, as observed in the electronic phase transitions in CeTe₃ and VO₂. We have shown that the electronic energy initially decays into selected phonon modes that ultimately drive the structural phase transitions. The relationship between electronic and structural phase transitions is more subtle. In CeTe₃, the two seem to be inseparable as demanded by the fundamental physics where the structural distortion is a central driver for the formation of charge-density waves, as the CDW gap size and structural distortion is directly correlated. This macroscopic cooperativity needs time to establish even though microscopically the two are intimately coupled, as shown in the transient nonequilibrium driven by impulsive electronic heating where the optical gap is temporarily closed, while the structural distortion recovers at a longer timescale. The fact that swift recovery of charge ordering occurs before the electronic energy is fully transferred to the lattice verifies the inherently cooperative nature between macroscopic electronic and structure orderings. In such a case, the strength of electron-phonon coupling can be evaluated based on the respective heat capacities and coupling timescales between the electron and CDW modes using 3TM framework. However, this scenario may not be applicable to other CDWs that are strongly electronically driven with strong excitonic nature, such as 1T-TiSe₂⁶ and 2H-TaSe₂^{113,114}, electron correlation enhancements, such as 1T-TaS₂⁴⁰ and 1T-TiSe₂¹⁷, or heavy Fermion behavior, such as KNi₂S₂¹¹⁵, where both electron-electron (hole) and electron-phonon interactions are at play. The effects of electron correlation on the coupling between collective structural and electronic phases are also seen. In a strongly correlation-driven electronic phase transition, the macroscopic cooperativity between the two might be coincidental, which could be driven by nonessential perturbations such as strain and doping, as indeed electrostatic doping has driven the structural phase out of equilibrium with the electronic one^{30,100} in VO₂. These perturbations can shift or strengthen the respective electron-electron or electron-phonon coupling, but are not the core driving mechanism for the formation of collective states.

In a related study of graphite, while there is no distinct electronic phase which is controlled directly by the electron-phonon coupling, the coupling hierarchy between the electrons and phonons can be as complex, suggesting that momentum (energy)-dependent nonequilibrium dynamics might be the result of restriction in the dynamical phase space of the excited carriers and phonons in a reduced FS topology. This is evidenced in the common existence of hot phonons mediating the energy flow seen in the three diversely different systems. This restriction then can afford functionality, especially

in cooperative systems, such as CeTe_3 and VO_2 . A subset of phonon modes are shown to control the majority of energy flow from electronic and lattice energies following the optical excitation. Optical control of these key pathways might result in ultrafast switching with reduced thermal dissipation. Generally, because of the restricted access to the full momentum phase space at short timescales, the transient nonequilibrium affords the description of different local temperatures for each subsets of thermal baths when the coupling timescales set by the electron-electron, electron-phonon, and phonon-phonon interactions are sufficiently different. This thermodynamic view is shown to be rather satisfactory in describing the CeTe_3 and VO_2 dynamics, but seems to be inadequate for graphite at the ultrashort timescales (≤ 500 fs). Extension of this thermodynamic view might be necessary in the general case, especially at the short timescales where electronic temperature cannot be seen as uniform in different momentum subspaces, and the quantum dynamical calculations, such as Hubbard-Holstein model¹¹⁶ and dynamical mean-field theory¹¹⁷, need to be invoked to account for electrodynamics and the nascent hot electron effects. In such circumstances, three-temperature model can be used as an approximation to estimate the effective temperatures for each subsets and deduce the effective coupling constants. Momentum-resolved spectroscopy and UEC are well poised to provide crucial information on the electron-phonon mechanism from the electronic and ionic perspectives, and because of the prevalence of hot phonons in low dimensional functional materials full parameter space characterization, including quasi-particles and collective modes in both electronic and lattice subsystems, are often necessary, as demonstrated here. Therefore, we foresee the development of a unified framework combining ultrafast crystallography, spectroscopy, and modeling as essential to provide crucial quantitative perspectives in the dynamical regimes to unravel the fundamental physics of a series of complex materials with competitive emerging properties.

Acknowledgment

The experimental results of CeTe_3 and VO_2 from ultrafast electron crystallography are obtained from references¹⁸ and³⁰. The authors acknowledge valuable discussions with Ryan A. Murdick, Subhendra D. Mahanti, Phillip M. Duxbury, Ramani K. Raman, David Tomanek, Christos D. Malliakas, Mercouri G. Kanatzidis, and Junqiao Wu. This work was supported by the DOE under grant DE-FG02-06ER46309.

-
- * Electronic address: ruan@pa.msu.edu
- ¹ W. Kohn, Phys. Rev. Lett. **2**, 393 (1959).
 - ² G. Gruner, Density Waves in Solids (vol. 89 of Frontiers in Physics, Addison-Wesley, Reading, MA 1994).
 - ³ F. Weber, S. Rosenkranz, J.-P. Castellán, R. Osborn, R. Hott, R. Heid, K.-P. Bohnen, T. Egami, A. H. Said, and D. Reznik, Phys. Rev. Lett. **107**, 107403 (2011).
 - ⁴ M.D. Johannes, I.I. Mazin, Phys. Rev. B **77**, 165135 (2008).
 - ⁵ J. A. Wilson, F. J. Di Salvo, and S. Mahajan, Adv. Phys. **50**, 1171 (2001).
 - ⁶ H. Cercellier, C. Monney, F. Clerc, C. Battaglia, L. Despont, M.G. Garnier, H. Beck, P. Aebi, L. Patthey, H. Berger, and L. Forro, Phys. Rev. Lett. **99**, 146403 (2007).
 - ⁷ B. Mansart, M.J.G. Cottet, T. Penfold, S. Dugdale, R. Tediosi, M. Chergui, and F. Carbone, Proc. Natl. Acad. Sci. USA **109**, 5603 (2012).
 - ⁸ F. Schmitt, P.S. Kirchmann, U. Bovensiepen, R.G. Moore, L. Rettig, M. Krenz, J.-H. Chu, N. Ru, L. Perfetti, D.H. Lu, M. Wolf, I.R. Fisher, and Z.-X. Shen, Science **321**, 1649 (2008).
 - ⁹ C.L. Smallwood, C. Jozwiak, W. Zhang, and A. Lanzara, Rev. Sci. Instrum. **83**, 123904 (2012).
 - ¹⁰ Y.H. Wang, D. Hsieh, E.J. Sie, H. Steinberg, D.R. Gardner, Y. S. Lee, P. Jarillo-Herrero, and N. Gedik, Phys. Rev. Lett. **109**, 127401 (2012).
 - ¹¹ R.D. Averitt, and A.J. Taylor, J. Phys. - Cond. Matt. **14**, R1357 (2002).
 - ¹² D.N. Basov, R.D. Averitt, D. van der Marel, M. Dressel, and K. Haule, Rev. Mod. Phys. **83**, 471 (2011).
 - ¹³ A.H. Zewail, Annu. Rev. Phys. Chem. **57**, 65 (2006).
 - ¹⁴ C.-Y. Ruan, Y. Murooka, R.K. Raman, R.A. Murrick, R.J. Worhatch, and A. Pell, Microsc. Microanal. **15**, 323(2009).
 - ¹⁵ German Sciani, R.J. Dwayne Miller, Rep. Prog. Phys. **74**, 096101 (2011).
 - ¹⁶ M. Eichberger, H. Schaefer, M. Krumova, M. Beyer, J. Demsar, H. Berger, G. Moriena, G. Sciani, and R.J.D. Miller, Nature **468**, 799 (2010).
 - ¹⁷ E. Mohr-Vorobeva, S.L. Johnson, P. Beaud, U. Staub, R. De Souza, C. Milne, G. Ingold, J. Demsar, H. Schaefer, and A. Titov, Phys. Rev. Lett. **107**, 036403 (2011).
 - ¹⁸ T.-R. T. Han, Z. Tao, S.D. Mahanti, K. Chang, C.-Y. Ruan, C.D. Malliakas, and M.G. Kanatzidis, Phys. Rev. B **86**, 075145 (2012).
 - ¹⁹ S. Hellmann, T. Rohwer, M. Kallane, K. Hanff, C. Sohrt, A. Stange, A. Carr, M.M. Murnane, H.C. Kapteyn, L. Kipp, M. Bauer, and K. Rossnagel, Nat. Comm. **3**, 1069 (2012).
 - ²⁰ N. Erasmus, M. Eichberger, K. Haupt, I. Boshoff, G. Kassier, R. Birmurske, H. Berger, J. Demsar, and H. Schwoerer Phys. Rev. Lett. **109**, 167402 (2012).
 - ²¹ A. Tomeljak, H. Schaefer, D. Stadter, M. Beyer, K. Biljakovic, and J. Demsar, Phys. Rev. Lett. **102**, 066404 (2009).
 - ²² R. Yusupov, T. Mertelj, V.V. Kabanov, S. Brazovskii, P. Kusar, J.-H. Chu, I.R. Fisher, and D. Mihailovic, Nature Phys. **6**, 681 (2010).
 - ²³ M.I. Kaganov, I.M. Lifshitz, and L.V. Tanatarov, Sov. Phys. JETP-USSR **4**, 173 (1957).
 - ²⁴ S.I. Anisimov, B.I. Kapeliov, and T.L. Perelman, Zhurnal Eksperimentalnoi i Teoreticheskoi Fiziki **66**, 776 (1974).
 - ²⁵ J.K. Chen, W.P. Latham, and J.E. Beraun, J. of Laser Appl. **17**, 63 (2005).
 - ²⁶ Z. Lin, L.V. Zhigilei, and V. Celli, Phys. Rev. B **77**, 075133 (2008).
 - ²⁷ T.P. Devereaux, T. Cuk, Z.X. Shen, and N. Nagaosa, Phys. Rev. Lett. **93**, 117004 (2004).
 - ²⁸ T. Cuk, D. H. Lu, X. J. Zhou, Z.-X. Shen, T. P. Devereaux, and N. Nagaosa, Phys. Stat. Sol. (b) **242**, 11 (2005).
 - ²⁹ G.F. Giuliani, and A.W. Overhauser, Phys. Rev. B **23**, 3737 (1981).
 - ³⁰ Z. Tao, T.-R. T. Han, S.D. Mahanti, P.M. Duxbury, F. Yuan, C.-Y. Ruan, K. Wang, and J. Wu, Phys. Rev. Lett. **109**, 166406 (2012).
 - ³¹ T. Kampfrath, L. Perfetti, F. Schapper, C. Frischkorn, and M. Wolf, Phys. Rev. Lett. **95**, 187403 (2005).
 - ³² F. Carbone, D.-S. Yang, E. Giannini, and A.H. Zewail, Proc. Natl. Acad. Sci. USA **105**, 20161 (2008).
 - ³³ N. Ru and I.R. Fisher, Phys. Rev. B **73**, 033101 (2006).
 - ³⁴ J. Demsar, K. Biljakovic, and D. Mihailovic, Phys. Rev. Lett. **83**, 800 (1999).
 - ³⁵ The calculation of electronic thermal conductivity follows the Wiedemann-Franz law. Lrtz is the Lorentz number, and $Lrtz=2.44 \times 10^{-8} \text{ W}\Omega \text{ K}^{-2}$.
 - ³⁶ N. Ru, C.L. Condron, G.Y. Margulis, K.Y. Shin, J. Laverock, S.B. Dugdale, M.F. Toney, and I.R. Fisher, Phys. Rev. B **77**, 035114 (2008).
 - ³⁷ D.A. Zocco, J.J. Hamlin, T.A. Sayles, M.B. Maple, J.-H. Chu, and I.R. Fisher, Phys. Rev. B **79**, 134428 (2009).
 - ³⁸ R. Venkatasubramanian, Phys. Rev. B **61**, 3091 (2000).
 - ³⁹ R.W. MacCormack, AIAA Paper, 69-354 (1969).
 - ⁴⁰ K. Rossnagel, J. Phys.: Condens. Matter **23**, 213001 (2011).
 - ⁴¹ J. Laverock, S. B. Dugdale, Zs. Major, M. A. Alam, N. Ru, I. R. Fisher, G. Santi, and E. Bruno, Phys. Rev. B **71**, 085114 (2005).
 - ⁴² H.-M. Eiter, M. Lavagnini, R. Hackl, E.A. Nowadnick, A.F. Kemper, T.P. Devereaux, J.-H. Chu, J.G. Analytis, I.R. Fisher, and L. Degiorgi, Proc. Nat. Acad. Sci. USA **110**, 64 (2013).
 - ⁴³ P. Kusar, T. Mertelj, V. V. Kabanov, J.-H. Chu, I. R. Fisher, H. Berger, L. Forro, and D. Mihailovic, Phys. Rev. B **83**, 035104 (2011).
 - ⁴⁴ G. Moos, C. Gahl, R. Fasel, M. Wolf, and T. Hertel, Phys. Rev. Lett. **87**, 267402 (2001).
 - ⁴⁵ Y. Ishida, T. Togashi, K. Yamamoto, M. Tanaka, T. Taniuchi, T. Kiss, M. Nakajima, T. Suemoto, and S. Shin, Sci. Rep. **1**, 64 (2011).
 - ⁴⁶ D.H. Reitze, H. Ahn, and M.C. Downer, Phys. Rev. B **45**, 2677 (1992).
 - ⁴⁷ M. Breusing, C. Ropers, and T. Elsaesser, Phys. Rev. Lett. **102**, 086809 (2009).
 - ⁴⁸ F. Carbone, G. Aubock, A. Cannizzo, F. van Mourik, K. Novoselov, A. Geim, and M. Chergui, Chem. Phys. Lett. **504**, 37 (2011).
 - ⁴⁹ C.S. Leem, B. J. Kim, Chul Kim, S. R. Park, T. Ohta, A. Bostwick, E. Rotenberg, H.-D. Kim, M.K. Kim, H.J. Choi, and C. Kim, Phys. Rev. Lett. **100**, 016802 (2008).
 - ⁵⁰ C.H. Lui, K.F. Mak, J. Shan, and T.F. Heinz, Phys. Rev. Lett. **105**, 127404 (2010).

- ⁵¹ J. Liu, R. Neumann, C. Trautmann, and C. Muller, Phys. Rev. B **64**, 184115 (2001).
- ⁵² M. Toulemonde private communication.
- ⁵³ J. Maultzsch, S. Reich, C. Thomsen, H. Requardt, and P. Ordejon Phys. Rev. Lett. **92**, 075501 (2004).
- ⁵⁴ S. Piscanec, M. Lazzeri, Francesco Mauri, A.C. Ferrari, and J. Robertson, Phys. Rev. Lett. **93**, 185503 (2004).
- ⁵⁵ Y. Liu, Longxiang Zhang, M. K. Brinkley, G. Bian, T. Miller, and T.-C. Chiang, Phys. Rev. Lett. **105**, 136804 (2010).
- ⁵⁶ K. Kang, D. Abdula, D.G. Cahill, and M. Shim, Phys. Rev. B **81**, 165405 (2010).
- ⁵⁷ S. Schafer, W. Liang, and A.H. Zewail, N. J. Phys. **13**, 063030 (2011).
- ⁵⁸ R.K. Raman, Y. Murooka, C.-Y. Ruan, T. Yang, S. Berber, and D. Tomanek, Phys. Rev. Lett. **101**, 077401 (2008).
- ⁵⁹ M. Harb, A. Jurgilaitis, H. Enquist, R. Nuske, C. v. Korff Schmising, J. Gaudin, S. L. Johnson, C. J. Milne, P. Beaud, E. Vorobeve, A. Caviezel, S. O. Mariager, G. Ingold, and J. Larsson, Phys. Rev. B **84**, 045435 (2011).
- ⁶⁰ K. Ishioka, M. Hase, M. Kitajima, L. Wirtz, A. Rubio, and H. Petek, Phys. Rev. B **77**, 121402R (2008).
- ⁶¹ T. Mishina, K. Nitta, and Y. Masumoto, Phys. Rev. B **62**, 2908 (2000).
- ⁶² E. Fritzer, and U. Funck, Carbon **16**, 85 (1978).
- ⁶³ G.R. Stewart, Rev. Sci. Instrum. **54**, 1 (1983).
- ⁶⁴ M.S. Dresselhaus, and G. Dresselhaus, Adv. Phys. **51**, 1-186 (2002).
- ⁶⁵ Z. Yao, C. L. Kane, and C. Dekker, Phys. Rev. Lett. **84**, 2941 (2000).
- ⁶⁶ A. Javey, J. Guo, M. Paulsson, Q. Wang, D. Mann, M. Lundstrom, and H. Dai, Phys. Rev. Lett. **92**, 106804 (2004).
- ⁶⁷ M. Lazzeri, S. Piscanec, F. Mauri, A. C. Ferrari, and J. Robertson, Phys. Rev. Lett. **95**, 236802 (2005).
- ⁶⁸ E. Pop, D. Mann, J. Cao, Q. Wang, K. Goodson, and H. Dai, Phys. Rev. Lett. **95**, 155505 (2005).
- ⁶⁹ M. Lazzeri and F. Mauri, Phys. Rev. B **73**, 165419 (2006).
- ⁷⁰ A. Barreiro, M. Lazzeri, J. Moser, F. Mauri, and A. Bachtold, Phys. Rev. Lett. **103**, 076601 (2009).
- ⁷¹ I. Meric, M. Y. Han, A. F. Young, B. Ozyilmaz, P. Kim, and K. L. Shepard, Nat. Nanotechnol. **3**, 654 (2008).
- ⁷² N. Bonini, M. Lazzeri, N. Marzari, and F. Mauri, Phys. Rev. Lett. **99**, 176802 (2007).
- ⁷³ S. Pagliara, G. Galimberti, S. Mor, M. Montagnese, G. Ferrini, M. S. Grandi, P. Galinetto, and F. Parmigiani, J. Am. Chem. Soc. **133**, 6318 (2011).
- ⁷⁴ F. Carbone, P. Baum, P. Rudolf, and A.H. Zewail, Phys. Rev. Lett. **100**, 035501 (2008).
- ⁷⁵ J. Kanasaki, E. Inami, K. Tanimura, H. Ohnishi, and K. Nasu, Phys. Rev. Lett. **102**, 087402 (2009).
- ⁷⁶ Y. Miyamoto, H. Zhang, and D. Tomanek, Phys. Rev. Lett. **104**, 208302 (2010).
- ⁷⁷ V. Eyert, Ann. Phys. (Leipzig) **11**, 650 (2002).
- ⁷⁸ L. Whittaker, C.J. Patridge, S. Banerjee, J. Phys. Chem. Lett. **2**, 745 (2011).
- ⁷⁹ A. Cavalleri, Th. Dekorsy, H.H.W. Chong, J.C. Kieffer, and R.W. Schoenlein, Phys. Rev. B **70**, 161102R (2004).
- ⁸⁰ A. Cavalleri *et al.*, Phys. Rev. Lett. **87**, 237401 (2001).
- ⁸¹ M.W. Haverkort *et al.*, Phys. Rev. Lett. **95**, 196404 (2005).
- ⁸² T.C. Koethe *et al.*, Phys. Rev. Lett. **97**, 116402 (2006).
- ⁸³ H.-T. Kim, Y.W. Lee, B.-J. Kim, B.-G. Chae, S.J. Yun, K.-Y. Kang, K.-J. Han, K.-J. Yee, and Y.-S. Lim, **97**, 266401 (2006).
- ⁸⁴ P. Baum, D.-S. Yang, A.H. Zewail, Science **318**, 788 (2007).
- ⁸⁵ C. Kubler, H. Ehrke, R. Huber, R. Lopez, A. Halabica, R. F. Haglund, Jr., and A. Leitenstorfer, Phys. Rev. Lett. **99**, 116401 (2007).
- ⁸⁶ D. J. Hilton, R. P. Prasankumar, S. Fourmaux, A. Cavalleri, D. Brassard, M. A. El Khakani, J. C. Kieffer, A. J. Taylor, and R. D. Averitt, Phys. Rev. Lett. **99**, 226401 (2007).
- ⁸⁷ M.M. Qazilbash, M. Brehm, B.-G. Chae, P.-C. Ho, G. O. Andreev, B.-J. Kim, S. J. Yun, A. V. Balatsky, M. B. Maple, F. Keilmann, H.-T. Kim, and D. N. Basov, Science **318**, 1750 (2007).
- ⁸⁸ M. Hada, K. Okimura, and J. Matsuo, Appl. Phys. Lett. **99**, 051903 (2011).
- ⁸⁹ W. T. Liu, J. Cao, W. Fan, H. Zhao, M. C. Martin, J. Wu, and F. Wang, Nano Lett. **11**, 466 (2011).
- ⁹⁰ T. L. Cocker, L. V. Titova, S. Fourmaux, G. Holloway, H.-C. Bandulet, D. Brassard, J.-C. Kieffer, M. A. El Khakani, and F. A. Hegmann, Phys. Rev. B **85**, 155120 (2012).
- ⁹¹ S. Wall, L. Foglia, D. Wegkamp, K. Appavoo, J. Nag, R.F. Haglund, Jr., J. Stahler, and M. Wolf, Phys. Rev. B **87**, 115126 (2013).
- ⁹² M.S. Laad, L. Craco, and E. Muller-Hartmann, Phys. Rev. B **73**, 195120 (2006).
- ⁹³ S. Biermann, A. Poteryaev, A.I. Lichtenstein, and A. Georges, Phys. Rev. Lett. **94**, 026404 (2005).
- ⁹⁴ V. Eyert, Phys. Rev. Lett. **107**, 016401 (2011).
- ⁹⁵ C. Weber, D.D. O'Regan, N.D.M. Hine, M.C. Payne, G.Kotliar, and P.B. Littlewood, Phys. Rev. Lett. **108**, 256402(2012).
- ⁹⁶ J. Cao *et al.*, Nat. Nanotechnol. **4**, 732 (2009).
- ⁹⁷ J. Wei, Z. Wang, W. Chen, and D.H. Cobden, Nat. Nanotechnol. **4**, 420 (2009).
- ⁹⁸ A.C. Jones, S. Berweger, J. Wei, D. Cobden, M. B. Raschke, Nano Lett. **10**, 1574 (2010).
- ⁹⁹ S. Lee, C. Cheng, H. Guo, K. Hippalgaonkar, K. Wang, J. Suh, K. Liu, and J. Wu, J. Am. Chem. Soc. **135**, 4850 (2013).
- ¹⁰⁰ M. Nakano, K. Shibuya, D. Okuyama, T. Hatano, S. Ono, M. Kawasaki, Y. Iwasa, and Y. Tokura, Nature **487**, 459 (2013).
- ¹⁰¹ B.-J. Kim, Y.W. Lee, S. Choi, J.-W. Lim, S.J. Yun, H.-T. Kim, T.-J. Shin, and H.-S. Yun, Phys. Rev. B **77**, 235401 (2008).
- ¹⁰² S. Zhang, J.Y. Chou, and L.J. Lauhon, Nano Lett. **9**, 4527 (2009).
- ¹⁰³ M. Marezio, D.B. McWhan, J.P. Remeika, and P.D. Dernier, Phys. Rev. B **5**, 2541 (1972).
- ¹⁰⁴ D.B. McWhan, M. Marezio, J.P. Remeika, and P.D. Dernier, Phys. Rev. B **10**, 490 (1974).
- ¹⁰⁵ T. Yao *et al.*, Phys. Rev. Lett. **105**, 226405 (2010).
- ¹⁰⁶ S.A. Kivelson, I.P. Bindloss, E. Fradkin, V. Oganessian, J.M. Tranquada, A. Kapitulnik, and C. Howard, Re. Mod. Phys. **75**, 1201 (2003).
- ¹⁰⁷ Q. Huang *et al.*, Phys Rev Lett **101**, 257003 (2008).
- ¹⁰⁸ C. de la Cruz *et al.*, Nature **453**, 899 (2008).
- ¹⁰⁹ J. Tao, R.P. Prasankumar, E.E.M. Chia, A.J. Taylor, and J.-X. Zhu, Phys. Rev. B **85**, 144302 (2012).
- ¹¹⁰ N. Gedik, D.-S. Yang, G. Logvenov, I. Bozovic, A.H. Zewail, Science **316**, 425 (2008).
- ¹¹¹ J. Tao, and J.-X. Zhu, Phys. Rev. B **81**, 224506 (2010).

- ¹¹² R. Cortes, L. Rettig, Y. Yoshida, H. Eisaki, M. Wolf, and U. Bovensiepen, Phys. Rev. Lett. **107**, 097002 (2011).
- ¹¹³ T. Valla, A.V. Fedorov, P.D. Johnson, J. Xue, K.E. Smith, and F.J. DiSalvo, Phys. Rev. Lett. **85**, 4759 (2000).
- ¹¹⁴ A. Taraphder, S. Koley, N.S. Vidhyadhiraja, and M.S. Laad, Phys. Rev. Lett. **106**, 236405 (2011).
- ¹¹⁵ J.R. Neilson, T.M. McQueen, A. Llobet, J. Wen, and M.R. Suchomel, Phys. Rev. B **87**, 045124 (2013).
- ¹¹⁶ G. De Filippis, V. Cataudella, E.A. Nowadnick, T.P. Devereaux, A.S. Mishchenko, and N. Nagaosa, Phys. Rev. Lett. **109** 176402 (2012).
- ¹¹⁷ M. Eckstein, and M. Kollar, Phys. Rev. B **78**, 205119 (2008).